PHOTONICS Research

Mode-conversion-based silicon photonic modulator loaded by a combination of lateral and interleaved p-n junctions

Omid Jafari,[1,*] Sasan Zhalehpour,[2] Wei Shi,[1] and Sophie LaRochelle[1]

[1]Centre d'optique, photonique et laser (COPL), Université Laval, Québec City, Québec, Canada
[2]Canada Research Center, Huawei Technologies Canada, Ottawa, Ontario, Canada
*Corresponding author: omid.jafari.1@ulaval.ca

Received 9 November 2020; revised 16 January 2021; accepted 2 February 2021; posted 2 February 2021 (Doc. ID 414400); published 19 March 2021

We experimentally demonstrate a silicon photonic modulator that can be loaded with a combination of lateral and interleaved p-n junctions to enhance its phase modulation. We use an asymmetric Bragg grating to introduce mode conversion in the active area, allowing the modulator to operate in reflection without introducing additional on-chip loss. With a compact footprint (phase shifter length of 290 μm), the modulator demonstrates a modulation speed up to 45 Gb/s with a bit error rate below the 7% forward-error-correction (FEC) threshold (up to 55 Gb/s with 20% FEC), and a low power consumption of 226 fJ/bit.

https://doi.org/10.1364/PRJ.414400

1. INTRODUCTION

Photonic integration leverages design kits of silicon photonic (SiP) components to achieve high yield and reduced costs using the mature complementary metal oxide-semiconductor (CMOS) manufacturing process. A key element of integrated transceivers is SiP modulators, which have received considerable attention during the last decade. SiP Mach–Zehnder modulators (MZMs) and microring modulators (MRMs) have thus been demonstrated with high-speed operation and high stability in the former case, and low energy per bit with an ultracompact footprint in the latter case [1–4]. Despite these attractive properties, the narrow optical bandwidth of MRMs makes them difficult to stabilize, while the long phase shifter MZMs are energy-hungry. Bragg grating modulators, through careful optimization of their structure, offer the potential to improve this performance trade-off, i.e., offering a compact solution with reduced stabilization requirements [5–7].

Analysis of Bragg grating modulators shows that operating the device in the reflection is more efficient than using it in transmission [8]. More specifically, when operated in reflection, the grating strength can be lower for a given optical modulation amplitude, thereby introducing less time delay and improving modulation speed [8]. However, operation in reflection is typically characterized by higher loss due to the lack of on-chip circulators. Therefore, the signal from Bragg grating modulators operated in reflection is typically retrieved by either an external circulator, adding complexity and cost, or by an on-chip splitter, e.g., a Y-junction that introduces an additional loss of 6 dB.

In Ref. [9], we proposed using asymmetric Bragg gratings to achieve modulation in reflection with low on-chip loss and without the need for circulators. The mode conversion introduced by the asymmetric Bragg grating allows one to direct the reflected signal to a drop port with low loss. In our initial work, we used an asymmetric Y-branch to filter the reflected mode, and phase modulation was achieved by a standard lateral p-n junction [10]. In this work, to optimize the phase modulation, we introduce a novel design of an asymmetric Bragg grating modulator loaded with a combination of lateral and interleaved (C-LI) p-n junctions. We experimentally show that the C-LI p-n junction increases the phase modulation by 67%, compared to the lateral p-n junction, with design features that respect the requirements of standard fabrication processes. We further propose an asymmetric directional coupler, instead of an asymmetric Y-branch, to reduce insertion loss and cross talk. This optimized design, with a phase shifter length of 290 μm, demonstrates modulation speeds up to 55 Gb/s, with an estimated power consumption of 226 fJ/bit.

2. DESIGN AND MODULATOR STRUCTURE

Figure 1(a) presents the modulator schematic and operating principle. It shows that the launched TE0 mode is guided into the asymmetric Bragg grating waveguide using a directional coupler and a taper. Thereafter, due to half-period offset between two sidewall gratings, contradirectional coupling converts the incident TE0 mode into a reflected TE1 mode. Then, the reflected signal is directed to the drop port using the

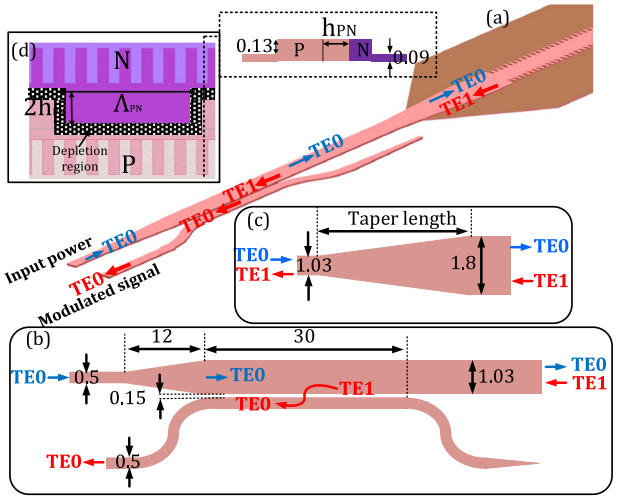

Fig. 1. Schematic of (a) the full modulator structure, (b) the asymmetric directional coupler, (c) the taper between the asymmetric directional coupler and the asymmetric Bragg structure, and (d) the asymmetric Bragg grating waveguide loaded by a C-LI p-n junction and its cross section. The parameter values are in micrometers.

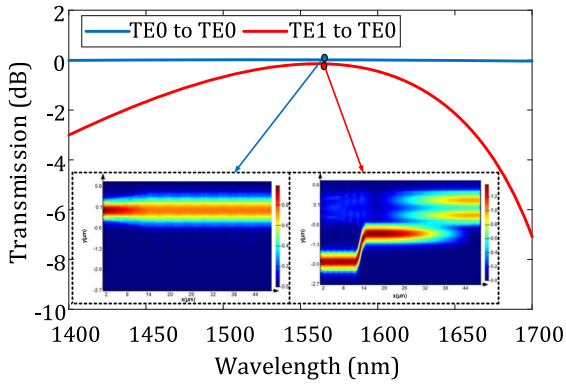

Fig. 2. Spectral response of the asymmetric directional coupler simulated in Lumerical-FDTD showing the transmission of the input TE0 mode to the through port (blue) and the transmission of the reflected TE1 mode to the drop port (red).

asymmetric directional coupler, shown in Fig. 1(b), that converts the TE1 mode to TE0 mode at the output. The combination of asymmetric Bragg grating and asymmetric directional coupler thus overcomes the need for an on-chip circulator.

A. Asymmetric Directional Coupler

Ideally, the asymmetric directional coupler should transmit all of the incident power launched in the TE0 mode to the TE0 mode of the multimode waveguide output, while all of the reflected power in the TE1 mode should be coupled to the TE0 mode of the drop port. Figure 1(b) shows the design of the asymmetric directional coupler consisting of a 500-nm-width input waveguide and a taper with a length of 12 μm followed by bus and drop waveguides with respective widths of 1.03 and 500 nm. The coupling section has a length of 30 μm and a gap of 150 nm. Design and simulations of the asymmetric coupler were performed using Lumerical-Mode and Lumerical-FDTD. Figure 2 shows the simulation results, showing negligible insertion loss for transmission of the TE0 through the device [see blue arrows in the Fig. 1(b), blue line and left inset in Fig. 2] and less than 0.5 dB loss when coupling the reflected TE1 to TE0 mode [see red arrows in the Fig. 1(b), red line and right inset in Fig. 2].

Finally, note that a taper, shown in Fig. 1(c), is placed between the directional coupler multimode output and the multimode waveguide with the asymmetric Bragg grating in order to insure mode-matching. Simulations showed that a taper length of at least 10 μm was required to guarantee low loss for both modes. We chose a 20 μm taper length.

B. Asymmetric Bragg Grating Waveguide

The asymmetric Bragg grating consists of a waveguide whose sidewall gratings are placed with a π phase shift, as shown in Fig. 1(d). This π phase shift suppresses the Bragg reflection of the fundamental TE0 mode but allows contradirectional coupling between the two TE0 and TE1 modes if the phase-matching condition is satisfied. The asymmetric grating is designed with a 50% duty cycle, lateral corrugations of 500 nm on each side, and a pitch of $\Lambda = 325$ nm in a ridge waveguide with an 800 nm width.

The modulation efficiency of this modulator strongly depends on the p-n junction position. For example, if a lateral p-n junction [shown in Fig. 3(a)] is placed at the middle of the waveguide (i.e., $h_{PN} = 0$), the overlap between the optical TE0 mode and the depletion region will be maximum. However, in this case, a low overlap between the optical TE1 mode and the depletion region will occur because the optical power for the TE1 mode field is close to zero in this region. Therefore, the total phase modulation, which depends on the refractive index change of both the TE1 and TE0 modes, will not be maximized. In Fig. 3(d), we examine the Bragg wavelength shift [i.e., $\Delta\lambda_{Bragg} = (\Delta n_0 + \Delta n_1)\Lambda$, where Δn_0 and Δn_1 are the refractive index change for TE0 and TE1 modes, respectively] as a function of the p-n junction offset (h_{PN}). It is seen that Δn_0 is maximum when the p-n junction is located at the middle of the waveguide ($h_{PN} = 0$ nm), while Δn_1 becomes maximum when the offset is $h_{PN} = 320$ nm. The Bragg wavelength shift therefore peaks at an offset of $h_{PN} = 250$ nm, where Δn_0 and Δn_1 reach a compromise. Note that we performed simulations considering an estimated doping concentrations of $N_A = 5 \times 10^{17}$ cm^{-3} and $N_D = 3 \times 10^{17}$ cm^{-3} for holes and electrons, respectively [11].

In Fig. 4, we examine the modulation of refractive indices for positive and negative junction offsets. As indicated, although the optical modes are symmetric with respect to the middle of the waveguide, index modulations for the TE0 (blue line) and for the TE1 (red line) are not due to unequal index modulations introduced by holes and electrons. Nevertheless, their sum values for optimum junction offset ($h_{PN} = 250$ nm) and its negative value ($h_{PN} = -250$ nm) are almost identical (see the blue dots marked on the black line in the Fig. 4). Given that the sum of them (i.e., $\Delta n_0 + \Delta n_1$) determines the Bragg wavelength modulation, we assume that the lateral p-n junctions can offer the same phase modulation if placed in one section with a positive optimum offset and in the next section with a negative optimum offset. Such a doping profile,

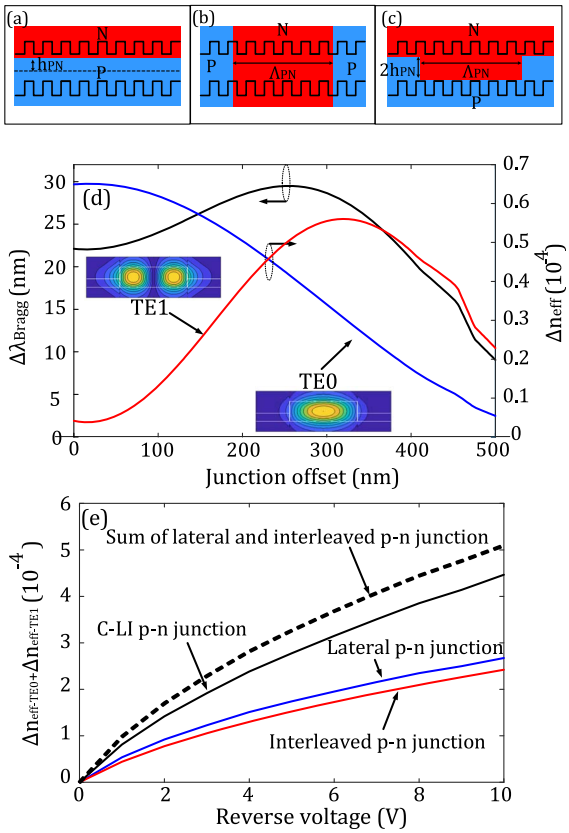

Fig. 3. Schematic of (a) lateral, (b) interleaved, and (c) C-LI p-n junctions; (d) refractive index variations for TE0 and TE1 modes, and the Bragg wavelength shift as a function of the PN junction offset at a reverse bias of 2 V for lateral p-n junctions; (e) sum of refractive index modulation for TE0 and TE1 modes ($\Delta n_0 + \Delta n_1$) as a function of reverse bias for different p-n junction profiles.

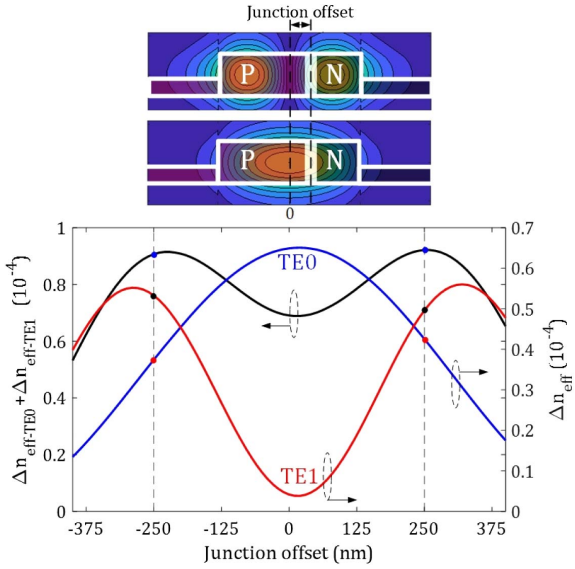

Fig. 4. Refractive index variations for TE0 (blue line) and TE1 (red line) modes as well as sum of them ($\Delta n_0 + \Delta n_1$) as a function of junction offset.

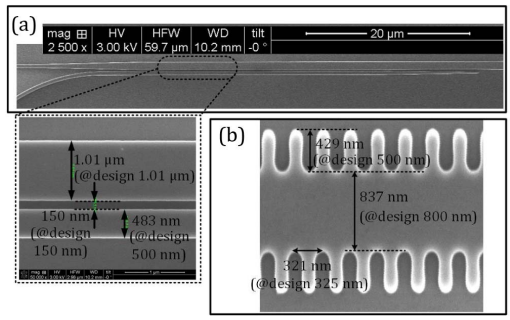

Fig. 5. SEM picture of (a) the directional coupler, and (b) the asymmetric Bragg grating waveguide.

with a half-period Λ_{PN}, is shown in Fig. 1(d). This doping profile helps to gain modulation enhancement because, in addition to the lateral p-n junction, it creates an additional phase modulation resulting from the presence of the interleaved section. In Fig. 3(e), we examine the refractive index variations of TE0 and TE1 modes ($\Delta n_0 + \Delta n_1$) as a function of the reverse voltage for the three doping shapes: lateral p-n junction with $h_{PN} = 250$ nm [Fig. 3(a)]; interleaved p-n junction with $\Lambda_{PN} = 1$ µm [Fig. 3(b)]; C-LI p-n junction with $h_{PN} = 250$ nm and $\Lambda_{PN} = 1$ µm [Fig. 3(c)]. For the interleaved and C-LI, the refractive index change is averaged over one doping period and simulations were done in MATLAB [12–14]. Figure 3(e) shows that a C-LI p-n junction introduces significantly more phase modulation than a lateral p-n junction but less than the sum of interleaved and lateral.

3. DEVICE CHARACTERIZATION

Modulators and test structures were fabricated in a multiproject wafer run (CMC Microsystems) using a standard 193-nm-lithography process at the Advanced Micro Foundry (AMF). The thickness of the silicon layer is 220 nm, and the thickness of buried oxide is 2 µm. The modulator phase shifters have a length of 290 µm (900 grating periods). Figures 5(a) and 5(b) show the scanning electron microscope (SEM) pictures of a fabricated directional coupler and asymmetric Bragg grating waveguide, respectively.

A. Asymmetric Directional Coupler

We experimentally evaluate the performance of the directional coupler using a four-port back-to-back test structure shown in the inset of Fig. 6. Figure 6(a) shows the spectra when the power is launched from Port 1. As expected, most power is captured from Port 2. The cross talk, i.e., the power from Port 3, is lower than 30 dB over the C-band. Also, the reflected power captured from Port 4 is negligible. In this case, there is no mode conversion, i.e., the TE0 mode is transmitted through the device (input waveguide, bus waveguide, and output waveguide). Figure 6(b) illustrates the results when the power is launched from Port 4. In this case, the mode conversion occurs at both directional couplers (i.e., the TE1 mode propagates in the bus waveguide) and most power exits from Port 3. The insertion loss is lower than 2 dB, and the cross talk (S24) is less

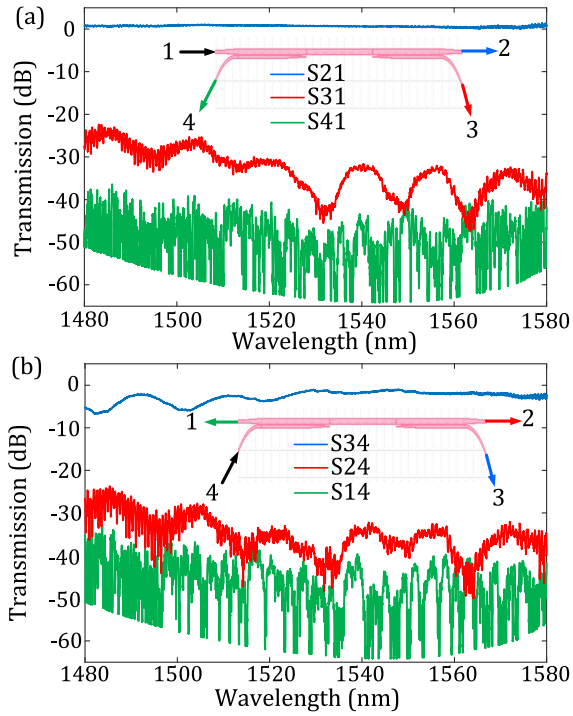

Fig. 6. Measured spectra of the asymmetric directional coupler when (a) the power is input in Port 1 and coupled to the TE0 mode in the multimode waveguide, and (b) the power is input in Port 4 and coupled to the TE1 mode in the multimode waveguide.

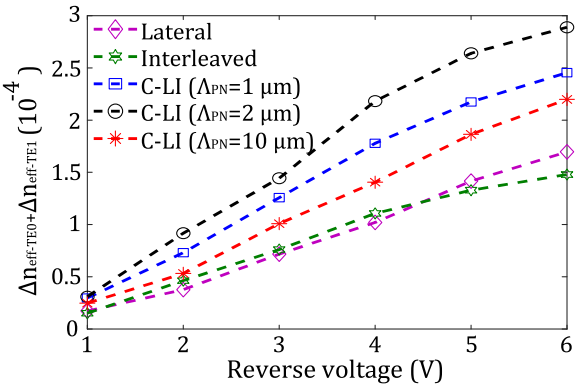

Fig. 7. Phase shift of asymmetric Bragg grating modulators with different p-n junction profiles as a function of the reverse voltage.

than 30 dB in the C-band. Finally, the reflected power detected at Port 1 is very small, close to the noise floor of the measurement.

Compared to the asymmetric Y-branch reported in Ref. [10], the directional coupler has a broader spectral response, lower loss over the C-band, and significantly less cross talk. The asymmetric Y-branch was characterized by an operating bandwidth of 15 nm, an insertion loss of 1.5 dB, and a cross talk of 7 dB, while the directional coupler improves these parameters to 35 nm, 1 dB, and 30 dB, respectively.

B. Modulator Characterization

We first evaluate the phase modulation enhancement using several modulators, with the five different doping profiles but with the same passive structure, fabricated on the same die. Figure 7 shows the refractive index variations measured from the shift in Bragg wavelength when applying reverse voltage for a lateral p-n junction with an h_{PN} of 250 nm, an interleaved p-n junction with a Λ_{PN} of 2 μm, and three C-LI junctions with a same h_{PN} of 250 nm and Λ_{PN} of 1, 2, and 10 μm. During measurement, the device slightly heats as the bias voltage is applied. We estimate that the temperature increase depends quadratically on the applied DC voltage with a maximum change of 1.3°C at a reverse voltage of 6 V. Note that the wavelength shift due to the change in the temperature is equal to 82 pm/°C [15]. This contribution was subtracted from all curves on Fig. 7. In terms of the phase modulation, the C-LI p-n junction outperforms the lateral p-n junction as well as the interleaved p-n junction. In addition, Fig. 7 illustrates that the C-LI junction with 2 μm pitch demonstrates the best performance, with 67% enhancement in phase modulation in comparison to the lateral p-n junction. The reason is that the smaller pitch (Λ_{PN}) for the p-n junction increases the number of interleaved sections, enhancing phase modulation. However, the pitch size is also limited by the fabrication process. Consequently, the C-LI junction with the smaller pitch (i.e., $\Lambda_{PN} = 1$ μm) shows a poorer phase modulation because it corresponds to the minimum feature size of the standard implantation process at AMF. Therefore, for the transmission experiment, we selected the modulator having a C-LI p-n junction with a pitch of $\Lambda_{PN} = 2$ μm.

Figure 8 zooms in on the reflected spectral response, at edge of the stop band, where this modulator is operated. The sharp response at the edge comes from employing strong corrugations in our design ($\Delta W = 500$ nm). However, the strong corrugations also lead to a high insertion loss of 2 dB. In addition, Fig. 8 indicates that similar to MRMs, the present modulator also has a narrow operating wavelength range. Hence, in order to fine-tune the operational wavelength, we placed a thermal element on the top of the asymmetric Bragg grating waveguide.

Figure 9 shows the electro-optic (EO) response of the modulator measured with a PNA network analyzer (Agilent N5227A 10 MHz–67 GHz). Note that we used a 50-Ω-terminated RF probe because of the lack of the on-chip termination.

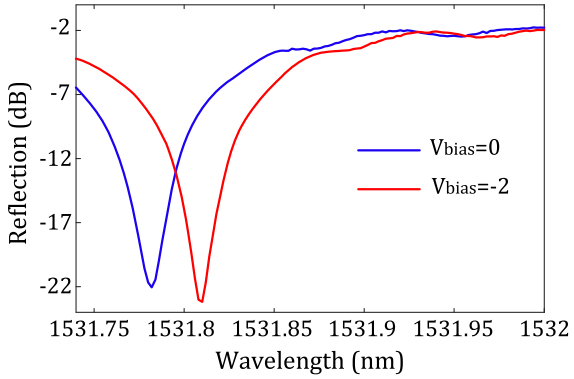

Fig. 8. Zoom in on the edge of the optical spectra, where the modulator is operated, of the asymmetric Bragg grating waveguide for reverse bias voltages of 0 and 2 V.

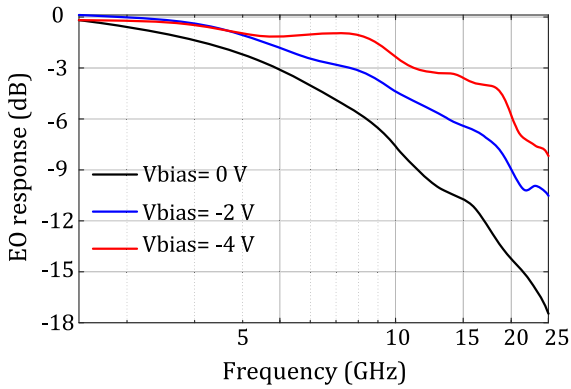

Fig. 9. Small-signal measurement of the asymmetric Bragg grating modulator for different reverse voltages.

It is seen that 3-dB EO bandwidth is 7.9 GHz for a reverse bias of 2 V. For a reverse bias voltage of 4 V, the small signal EO bandwidth is increased to 11.2 GHz; however, the large signal modulation efficiency is reduced, and therefore we opted for a reverse bias voltage of 2 V for the transmission experiments. Compared to lateral p-n junctions, the C-LI p-n junctions enhance the refractive index modulation via lengthening the depletion region along the electrode, which increases the junction capacitance and therefore the resistance-capacitance (RC) time constant. Note that in the present modulator, the EO bandwidth is limited not only by the RC time constant of the lumped electrode, but also by the response time of the strong grating structure characterized by an increased group velocity near the band edge. Slow light has the benefit of increasing the interaction time between the optical wave and the uniform RF voltage along the lumped electrode [11].

We tested the large signal response of the modulator by measuring the bit error rate (BER) using the setup shown in Fig. 10. We first generated a pseudorandom binary sequence (PRBS) with a length of $2^{15}-1$ using a bit pattern generator (SHF 12103 A). The signal was amplified with an RF amplifier (bandwidth of 50 GHz and V_{pp} of 5 V) and applied to the modulator using a bias-T (bandwidth of 50 GHz) that combined the RF signal and DC bias voltage ($V_{bias} = -2$ V). Considering a lumped electrode with a length of 290 μm, the total capacitance is estimated to be 36.25 fF at the reverse bias of 2 V [3]. The energy consumption per bit is thus calculated as $E_b = CV_{pp}^2/4 = 226$ fJ/bit.

In the optical part, we set the laser power to 15 dBm and adjusted the polarization with a polarization controller before coupling the light into the chip. After modulation, the signal was amplified by an erbium-doped fiber amplifier (EDFA), followed by a tunable optical bandpass filter with a fixed bandwidth of 0.7 nm. The output optical signal was converted to an electrical signal using a photodetector (SHF 41211 with a 32 GHz bandwidth) and then digitized by a real-time oscilloscope (RTO) with a sampling rate of 80 GSa/s and bandwidth of 60 GHz. At the receiver side (Fig. 10), the digital signal processing consisted of filtering [10th order super-Gaussian low-pass filter (LPF)], resampling, time synchronization, and downsampling. The BER is calculated with and without using a decision-directed minimum mean square error (DD-MMSE) equalizer with 2^4 taps. The signal is demapped for BER calculation. Figure 11 presents the BER measurement results as a function of the received power, showing that the modulator

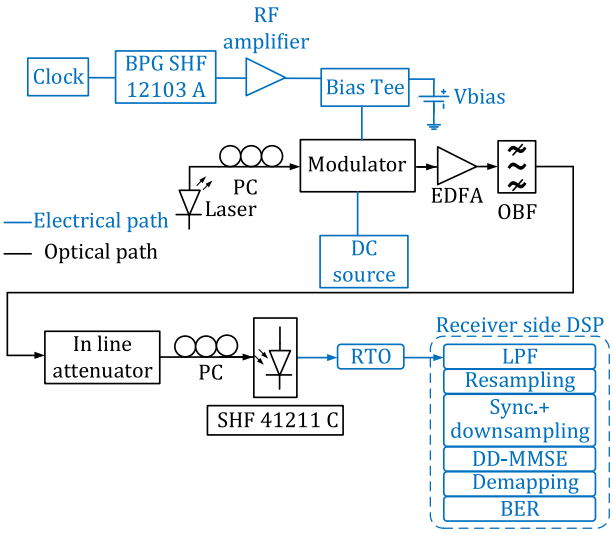

Fig. 10. Block diagram of the experimental setup.

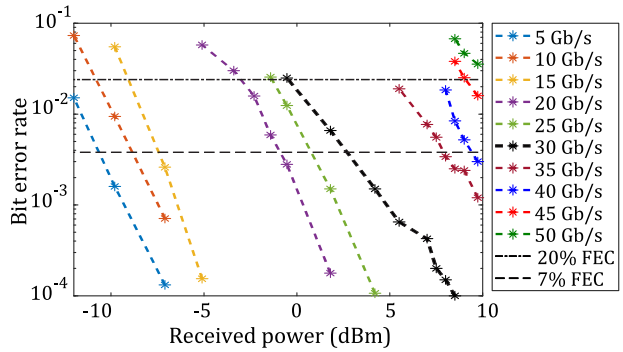

Fig. 11. BER as a function of the received power for different modulation speeds.

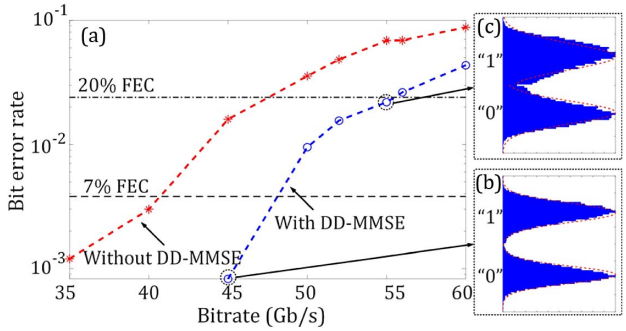

Fig. 12. (a) Measured BER as a function of bitrate without and with applying DD-MMSE equalizer; histograms of detected bits (one sample per symbol) used for BER calculation at bitrates of (b) 45 Gb/s and (c) 55 Gb/s. The dashed lines show the Gaussian distributions in (b) and (c).

can reach a speed of 45 Gb/s with 20% forward error correction (FEC) without DD-MMSE. Figure 12(a) also displays BER after applying a DD-MMSE equalizer at the maximum received power. Using a blind equalizer, transmission speeds up to 55 Gb/s can be reached with 20% FEC. Figures 12(b) and 12(c) show histograms of the detected bits at modulation speeds of 45 Gb/s and 55 Gb/s, respectively, presenting the quality of eye openings.

4. CONCLUSION

We presented a mode-conversion-based SiP modulator that takes advantage of lateral and interleaved p-n junctions simultaneously to enhance phase modulation. The modulator gains a 67% improvement in the phase modulation when loaded by the C-LI p-n junction compared to the lateral one. We employed an asymmetric Bragg grating waveguide to convert the incident TE0 mode to a reflected TE1 mode in order to direct the modulated signal to a drop port by using an asymmetric directional coupler. The whole structure therefore acts similarly to an on-chip circulator and avoids the usually high insertion loss of Bragg grating modulators. The experimentally demonstrated modulator had a phase shifter length of 290 μm, an insertion loss of 2 dB, and power consumption of 226 fJ/bit. The modulator operated up to 45 Gb/s (55 Gb/s) with BER below the 7% (20%) FEC threshold, showing a great potential for high-speed, low-cost, power-efficient transmissions.

Funding. Natural Sciences and Engineering Research Council of Canada and Huawei Canada through a Partnership (CRDPJ 538381-18).

Acknowledgment. The authors thank CMC Microsystems for the fabrication subsidy and MPW service.

Disclosures. The authors declare no conflicts of interest.

REFERENCES

1. M. Streshinsky, A. Ayazi, Z. Xuan, A. E.-J. Lim, G.-Q. Lo, T. Baehr-Jones, and M. Hochberg, "Highly linear silicon traveling wave Mach-Zehnder carrier depletion modulator based on differential drive," Opt. Express **21**, 3818–3825 (2013).
2. J. Sun, R. Kumar, M. Sakib, J. B. Driscoll, H. Jayatilleka, and H. Rong, "A 128 Gb/s PAM4 silicon microring modulator with integrated thermo-optic resonance tuning," J. Lightwave Technol. **37**, 110–115 (2019).
3. H. Sepehrian, J. Lin, L. A. Rusch, and W. Shi, "Silicon photonic IQ modulators for 400 Gb/s and beyond," J. Lightwave Technol. **37**, 3078–3086 (2019).
4. R. Dubé-Demers, S. LaRochelle, and W. Shi, "Ultrafast pulse-amplitude modulation with a femtojoule silicon photonic modulator," Optica **3**, 622–627 (2016).
5. O. Jafari, H. Sepehrian, S. LaRochelle, and W. Shi, "High-efficiency silicon photonic modulator using coupled Bragg grating resonators," J. Lightwave Technol. **37**, 2065–2075 (2019).
6. O. Jafari, W. Shi, and S. Larochelle, "Mach-Zehnder silicon photonic modulator assisted by phase-shifted Bragg gratings," IEEE Photon. Technol. Lett. **32**, 445–448 (2020).
7. A. Brimont, D. J. Thomson, F. Y. Gardes, J. M. Fedeli, G. T. Reed, J. Martí, and P. Sanchis, "High-contrast 40 Gb/s operation of a 500 μm long silicon carrier-depletion slow wave modulator," Opt. Lett. **37**, 3504–3506 (2012).
8. A. D. Simard and S. LaRochelle, "A dynamic model of silicon Bragg grating modulators," IEEE J. Sel. Top. Quantum Electron. **22**, 107–115 (2016).
9. O. Jafari, W. Shi, and S. LaRochelle, "Silicon photonic modulator using mode conversion with asymmetric sidewall Bragg gratings," in *IEEE 15th International Conference on Group IV Photonics (GFP)* (IEEE, 2018), pp. 1–2.
10. O. Jafari, J. Lin, W. Shi, and S. LaRochelle, "Mode-conversion-based silicon photonic modulator using asymmetric Bragg grating and Y-branch," in *European Conference on Optical Communication* (ECOC, 2019), pp. 1–2.
11. O. Jafari, W. Shi, and S. Larochelle, "Efficiency-speed tradeoff in slow-light silicon photonic modulators," IEEE J. Sel. Top. Quantum Electron. **27**, 3400611 (2020).
12. L. Chrostowski and M. E. Hochberg, *Silicon Photonics Design* (Cambridge University, 2015).
13. R. Dube-Demers, J. St-Yves, A. Bois, Q. Zhong, M. Caverley, Y. Wang, L. Chrostowski, S. Larochelle, D. V. Plant, and W. Shi, "Analytical modeling of silicon microring and microdisk modulators with electrical and optical dynamics," J. Lightwave Technol. **33**, 4240–4252 (2015).
14. H. Bahrami, H. Sepehrian, C. S. Park, L. A. Rusch, and W. Shi, "Time-domain large-signal modeling of traveling-wave modulators on SOI," J. Lightwave Technol. **34**, 2812–2823 (2016).
15. N. N. Klimov, S. Mittal, M. Berger, and Z. Ahmed, "On-chip silicon waveguide Bragg grating photonic temperature sensor," Opt. Lett. **40**, 3934–3936 (2015).